PCCP

RSC Publishing

PAPER

Gamma-radiolysis-assisted cobalt oxide nanoparticle formation

Cite this: *Phys. Chem. Chem. Phys.*, 2013, **15**, 1014

L. M. Alrehaily,[a] J. M. Joseph,[a] M. C. Biesinger,[b] D. A. Guzonas[c] and J. C. Wren*[a]

Received 4th September 2012,
Accepted 7th November 2012

DOI: 10.1039/c2cp43094k

www.rsc.org/pccp

The formation of Co_3O_4 nano-scale colloid particles by gamma irradiation of $CoSO_4$ solutions was investigated. Solutions of 0.2–0.3 mM $CoSO_4$ at pH 6.0 and 10.6 (air-saturated and Ar-purged) were irradiated at an absorbed dose rate of 5.5 kGy h^{-1}. The resulting concentrations of H_2, H_2O_2, Co^{II} and Co^{III} species in solution and the chemical composition and sizes of particles that were formed were measured as a function of irradiation time. Particle formation was observed only for initially air-saturated $CoSO_4$ solutions at pH 10.6. Analysis of the particle formation as a function of irradiation time shows that the particles evolve from $Co(OH)_2$ to CoOOH and then to Co_3O_4. The radiolytic oxidation of Co^{II} to Co^{III} was completed in 100 min and the chemical composition of the final particles was identified as Co_3O_4 by XPS, Raman and UV-Vis spectroscopy. Transmission electron microscopy (TEM) images show the final particles are approximately uniform in size, ranging from 8 to 20 nm. A mechanism is proposed to explain the particle formation. A key factor is the low solubility of $Co(OH)_2$ in air-saturated solutions at high pH. This mechanism for particle formation is compared with the mechanism previously reported for the radiolytic formation of γ-FeOOH nanoparticles.

1. Introduction

Recently synthesis of nano-scale structured transition metal oxides has been an area of active research due to the many technological applications of such oxide particles. The magnetic, catalytic, optical, and electronic properties of these metal oxides are determined by the size, structure and shape of the particles that they form.[1,2] Nanoparticles containing magnetic materials (such as iron, nickel and cobalt oxides) have potential applications in medical biotechnology, drug delivery and hyperthermic cancer treatment. They can also be used as contrast agents for magnetic resonance imaging (MRI).[3–7] This type of oxide is a magnetic p-type semiconductor with a cubic spinel crystal structure in which Co^{II} occupies the tetrahedral sites and the octrahedral sites are occupied by Co^{III}.[8] The properties of Co_3O_4 nanoparticles make them promising materials for electronic devices,[9] gas sensors,[10] magnetic materials,[11] electrochromic devices,[12] electrochemical anodes for sensors,[13] high temperature selective absorbers of solar radiation[14] and anode materials for rechargeable Li ion batteries.[1] Cobalt nanoparticles have also been proposed for use as an alternative to iron oxide nanoparticles as the contrast agent for MRI due to their greater impact on proton relaxation times.[1,15]

Cobalt oxide nanoparticles have been synthesized by different techniques including spray pyrolysis,[16] chemical vapour deposition,[17] sol–gel techniques,[18] pulsed laser deposition,[19] thermal decomposition of solid cobalt nitrate,[20] and hydrothermal synthesis.[1] These methods are either complex or require chemically harsh conditions and/or high processing temperatures for the synthesis of nano-scale crystalline Co_3O_4 particles. Radiolytic particle formation is a promising new technique for the synthesis of Co_3O_4 nanoparticles that avoids the need for chemically and thermally extreme conditions.

The potential formation of insoluble cobalt particles is also a particular concern for water-cooled nuclear reactors. Corrosion of metal alloys (and particularly Co-based alloys such as Stellites) can release dissolved Co ions into the reactor coolant water. Dissolved Co species can deposit in the reactor core where neutron activation can convert ^{59}Co to radioactive ^{60}Co. Subsequent resuspension/dissolution of the ^{60}Co and its transport by the coolant to out-of-core piping where it can redeposit can give rise to high radiation fields around system piping. Radiolytic conversion of dissolved ^{60}Co to colloidal particles will affect the transport and deposition of this radioactive isotope.

[a] *Department of Chemistry, The University of Western Ontario, London, Ontario, Canada N6A 5B7. E-mail: jcwren@uwo.ca; Fax: +1-519-661-3022; Tel: +1-519-661-2111 ext 86339*

[b] *Surface Science Western, The University of Western Ontario, London, Ontario, Canada N6G 0J3*

[c] *Atomic Energy of Canada Limited, Chalk River Laboratories, Chalk River, Ontario, Canada K0J 1J0*

Understanding the mechanisms for the formation of cobalt particulates is particularly important because of the radiological hazard posed by the formation of ^{60}Co.[21,22] On-line purification systems are used to control the concentrations of dissolved ions (using ion exchange resins) and particulates (using mechanical filters) in the coolant; the efficacy of filters for particle removal depends on the size of the particles present. Therefore, it is important to understand the various mechanisms that can convert dissolved Co species to particles.

Ionizing radiation includes high energy charged particles (such as α-particles and fast electrons) and electromagnetic radiation (x- and γ-rays). Due to its high energy (typically greater than 10 keV), when passing through matter, individual radiation particles or photons lose their energy continuously through a large number of collisions, mostly with electrons in the matter. The initial interaction of ionizing radiation with matter is thus to ionize the molecules or atoms on its track. Since the interaction is indiscriminant, radiolysis is considered as a non-selective, solvent-oriented process.[23,24] This contrasts with the selective, solute-oriented process that occurs in photolysis, where the energy of photons is on the order of a few eVs and can be tuned to the excitation energy of a target solute molecule. One important implication of this difference is that the reactions of dilute chemical species in water exposed to ionizing radiation occur primarily *via* reactions with radiolytic decomposition products of the solvent water.[24] Their direct interaction with incident radiation is negligible.

The initial consequence of each collision between a radiation particle and a water molecule is to form ion pairs ($H_2O^{\bullet+}$ and e^-_{hot}) or excited species (H_2O^*) along the radiation track where e^-_{hot} represents an energetic electron.[23,24] These hot electrons may themselves have sufficient energy to produce secondary ion pairs ($H_2O^{\bullet+}$ and e^-) and excited species before they are thermalized. Any secondary ionization they produce will be situated close to the original ionization (within a few nm or a few atom lengths) in a small cluster, or spur, of excited and ionized species. For water molecules, typically 2–3 ion pairs or excited species are formed in a spur. These energetic species undergo a range of chemical reactions as the spur expands. The distribution of radiolytic decomposition products of water becomes homogeneous along the radiation track on a time scale on the order of 10^{-7} s. The water decomposition products at this stage are referred to as the primary radiolysis products; while they are not the first species formed upon absorption of radiation energy, they are the first set of relatively stable, longer-lived species.

For a given type of radiation, the chemical yields of the primary radiolysis products at this stage depend mainly on the net absorption energy and, hence, the primary yields are expressed in *G*-values or the number of molecules produced per absorbed energy. The primary yields depend on the type of radiation and solvent properties. For the γ-radiolysis at room temperature, the primary products and their yields (in bracket in units of μmol J^{-1}) are:[23]

$$H_2O \xrightarrow{\sim\sim} {}^{\bullet}OH\ (0.26),\ {}^{\bullet}e_{aq}^{-}(0.26),\ {}^{\bullet}H(0.06),\ H_2(0.045),\ H_2O_2(0.075),\ H^+(0.26) \quad (1)$$

These chemical yields per unit energy input are very high. Such high yields, particularly for the radicals, cannot be obtained by thermal processes. Gamma-radiolysis is the most effective way of producing these reactive species. Due to the long penetration depth of a typical γ-ray in water (~20 cm for a half reduction in intensity), these species are also produced uniformly over a large volume of water. The high yields and the uniform production of the chemically reactive species at room temperature can provide ideal conditions for certain chemical reactions.

The primary radiolysis products continue to react with each other to form secondary products such as $^{\bullet}HO_2$, O_2 and $^{\bullet}O_2^-$ and eventually the stable products H_2, O_2 and H_2O_2. Under continuous irradiation, in pure water, the concentrations of radiolysis products quickly reach a pseudo-equilibrium state where the steady-state concentrations of the radiolysis products depend on radiation energy absorption rate, the solution pH, and temperature.[24,25] The radiolysis products are highly redox active and include both oxidizing (*e.g.*, $^{\bullet}OH$, H_2O_2 and O_2) and reducing (*e.g.*, $^{\bullet}H$, $^{\bullet}e_{aq}^-$ and $^{\bullet}O_2^-$) species. These species can readily interact with dissolved transition metal ions to change their oxidation states. Since the solubility of a transition metal ion can vary by several orders of magnitude depending on its oxidation state, reactions that can alter the oxidation state can control the concentrations of metal ions in solution. Conversion of dissolved metal species to oxidation states with low solubilities can lead to condensation and the formation of colloidal particles.

We have previously studied the formation of γ-FeOOH nanoparticles using steady-state radiolysis.[26] This study has shown that radiolytic oxidation of $Fe^{II}(aq)$ to less soluble $Fe(OH)_3$ provides nucleation sites for particle growth and that this oxidation is very fast. Subsequently ferrous ions are continuously oxidized and adsorbed on the nucleates, growing into nano-scale γ-FeOOH particles. The final size and morphology of the particles is regulated by the radiolytically induced steady-state redox conditions at the water–solid particle interface and the phase of the oxide.

This work reports on the behaviour of Co-containing solutions when exposed to γ-radiation and the formation of Co_3O_4 nanoparticles. The effects of pH and dissolved oxygen are investigated. Similarities and differences in particle formation and growth in the iron and cobalt systems are discussed.

2. Experimental

Cobalt solutions (0.2 and 0.3 mM) were prepared by dissolving high-purity cobalt(II) sulfate obtained from Sigma-Aldrich (purity ≥ 99%). All solutions were freshly prepared with water purified using a NANOpure Diamond UV ultrapure water system with a resistivity of 18.2 MΩ cm. The pH was adjusted to 6.0 and 10.6 using a concentrated NaOH solution. These pH values were chosen based on the solubilities of Co^{II} and Co^{III} species.[27]

The solubility of Co^{II} is at a minimum ($\sim 10^{-6}$ M) at pH 10.6 whereas it is several orders of magnitude higher (~ 1 M) at pH 6.0, see further discussion in Section 3.3. The solutions were either aerated by purging with high purity air (Praxair) or de-aerated by purging with Ar for one hour. Using a syringe, the test solution was transferred to a pre-sealed 20 ml vial leaving no headspace. The sample vials were irradiated in a ^{60}Co gamma cell (MDS Nordion) as described in a previous paper.[25] The gamma source provided a uniform absorption dose rate of 5.5 kGy h^{-1} in the water samples at the time of this study.

Following irradiation for the desired period, a series of chemical analyses of solution species were first performed. Colloid particles were then collected for various particle analyses. For the analysis of dissolved H_2 and O_2, one half (10 ml) of the irradiated test solution was transferred to a new 20 ml vacuum-sealed vial using a gas-tight syringe. Equilibration of the gas concentrations in the headspace above the solution with the gases in the aqueous phase was quickly established. A gas sample was extracted from the headspace using a gas-tight syringe with a Luer lock (Agilent Technologies) and was analyzed using gas chromatography with a thermal conductivity detector (GC-TCD, 6580 Agilent Technologies) as discussed elsewhere in detail.[25] The solutions were first analyzed for Co^{III} species by direct UV-VIS absorption (BioLogic Science Instruments). The solution cobalt species and H_2O_2 were subsequently quantified by colorimetric analysis.

The total concentration of Co^{III} present in the sample (dissolved or dispersed as a colloidal solid) was determined by reacting the sample with 4-(2-pyridylazo) resorcinol (PAR) to form a coloured complex that absorbs light at 510 nm with a molar extinction coefficient of 5.6×10^4 M^{-1} cm^{-1}.[28] To determine the concentration of Co^{II} present, the Co^{II} in the sample was first oxidized to Co^{III} using a 3% hydrogen peroxide solution and then the solution was heated to 100 °C in a boiling water bath to boil off any unreacted hydrogen peroxide. The Co^{III} concentration of this solution was then determined by the PAR method. The calibration curve for Co^{II} in the concentration range of 5 μM to 1 mM obtained by this method is shown in Fig. 1. The difference between the total cobalt concentration (after oxidation) and the concentration of Co^{III} determined prior to the hydrogen peroxide treatment was taken to be the concentration of Co^{II} in the solution phase. Using this method, the detection limits for both $[Co^{II}]$ and $[Co^{III}]$ were 1 μM.[28] Note that although we started our tests with 0.2 to 0.3 mM $CoSO_4$ solutions, the total amount of Co found in solution at pH 10.6 was actually less due to the loss of some Co through precipitation. The concentrations determined by the PAR method including the initial Co^{II} concentration, $[Co^{II}(sol)]_0$ are used throughout this paper.

The concentration of hydrogen peroxide in the test solution was determined by the Ghormley tri-iodide method[29] in which I^- is oxidized to I_3^- by H_2O_2 in the presence of ammonium molybdate as a catalyst, followed by spectrophotometric measurement of the I_3^- concentration; I_3^- has a maximum absorption at 350 nm with a molar extinction coefficient of 25 500 M^{-1} cm^{-1}.[30] We tested for and observed no oxidation of I^- to I_3^- by Co(III) in our test solutions.

Particles were collected from the sample vials for analyses by transmission electron microscopy (TEM), X-ray photoelectron spectroscopy (XPS) and Raman spectroscopy. For TEM the particles were collected by dipping a carbon-coated copper grid into the irradiated test solution and drying the sample grid in air. Samples for the XPS and Raman analyses were collected by centrifuging the solution and then drying the precipitate on a glass plate in an Ar-purged glove box. The sizes and shapes of the particles were measured using TEM with the microscope operating at 80 keV. X-ray photoelectron spectra were acquired on a Kratos AXIS Nova spectrometer using monochromatic Al K(alpha) radiation and operating at 210 W, with a base pressure of 10^{-8} Pa. Raman scattering measurements to determine the particle chemical composition were performed using a Renishaw model 2000 Raman Spectrometer with a laser excitation wavelength of 633 nm.

3. Results and discussion

3.1 Solution analyses

No conversion of dissolved Co^{II} to particles was observed at pH 6.0 either in the absence or presence of dissolved oxygen; see further discussion on the effect of pH in Section 3.3. Photographs of solutions that initially contained 0.32 mM $Co^{II}(sol)$ at pH 10.6, irradiated for different times, are shown in Fig. 2. Note that for the photographs the solutions were transferred to new, clear sample vials because the test sample vials darken when exposed to γ-radiation. The corresponding UV-Vis spectra of the test solutions are shown in Fig. 3. The pre-irradiated $CoSO_4$

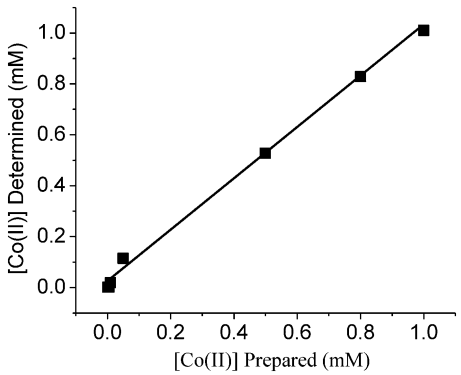

Fig. 1 Calibration curve obtained for $[Co^{II}]$ using the method used in the study.

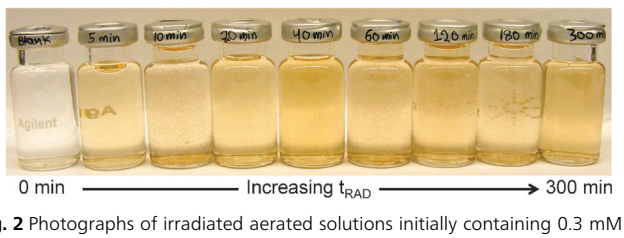

Fig. 2 Photographs of irradiated aerated solutions initially containing 0.3 mM $CoSO_4$ at pH 10.6.

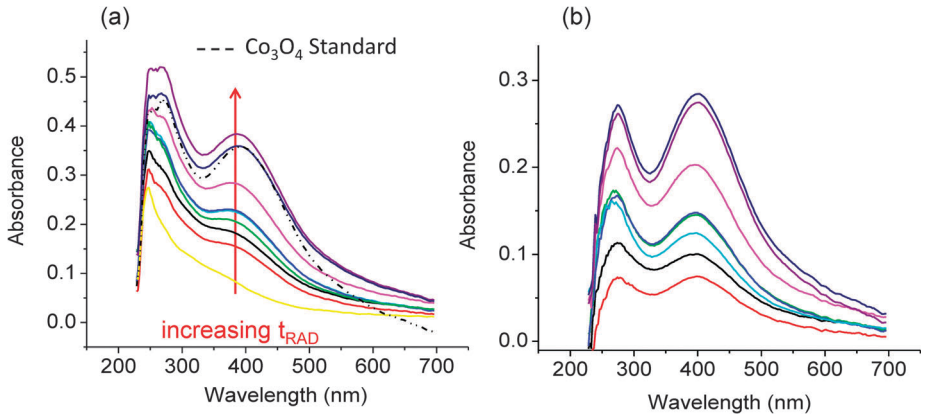

Fig. 3 UV-Vis spectra of irradiated aerated solutions initially containing 0.3 mM $CoSO_4$ at pH 10.6: (a) raw spectra and (b) empty-cell background-subtracted spectra. The reference spectrum of Co_3O_4 is shown as the dashed curve.

solution is colorless but the sample vial contains some precipitate at the bottom due to the conversion of some of the $CoSO_4$ to insoluble $Co(OH)_2$. With increasing irradiation time, t_{RAD}, the solution becomes increasingly brown in colour and more opaque. The amount of precipitate appears to increase with t_{RAD} up to ~60 min. After this time, the amount of precipitate appears to decrease (not quantitatively determined) while the solution continued to darken.

The UV-Vis spectra of the test solutions show increases in the intensities of absorption bands with maxima at ~280 and 400 nm, Fig. 3a. These spectra match very well with a reference spectrum taken with a solution that was prepared with dispersed Co_3O_4 particles. The Co_3O_4 used for the reference spectrum was purchased from Alfa Aesar and TEM analysis showed that the diameter of the particles was in the range of 8–20 nm. The similarity indicates that the irradiated test solutions contain Co_3O_4 particles and that the colloidal particle density increases with irradiation time. The good agreement between the reference spectrum and the test solution spectra also indicates that Co_3O_4 is the only colored species present. The other Co^{III} species, CoOOH, does not absorb in the 200 to 700 nm range.

The peak intensity of the background-subtracted band centered at ~400 nm is plotted as a function of t_{RAD} in Fig. 4. These results are compared in the same figure with the concentrations of Co^{III} determined by the PAR method. The two sets of data match very well except at long irradiation times (>250 min) in deaerated solutions. Compared to the aerated solution cases, the radiolytic conversion of Co^{II}(sol) to Co_3O_4 in deaerated solutions is negligible at pH 10.6.

The change in the oxidation state of the cobalt in solution as a function of t_{RAD} is shown in Fig. 5. The [Co^{III}(sol)] increases while the [Co^{II}(sol)] decreases before they reach the near plateau regions. (The sudden drop in log [Co^{II}(sol)] at 200 min is attributed to a continuous linear decrease in [Co^{II}(sol)] with time and not due to a change in the mechanism.) However, the total cobalt concentration in solution at any given time is not equal to [Co^{II}(sol)]$_0$. This discrepancy can be better appreciated in Fig. 5b where the change in [Co^{II}(sol)] (Δ[Co^{II}(sol)] = [Co^{II}(sol)]$_0$ − [Co^{II}(sol)]) is shown as well as the curve for [Co^{III}]. The discrepancy

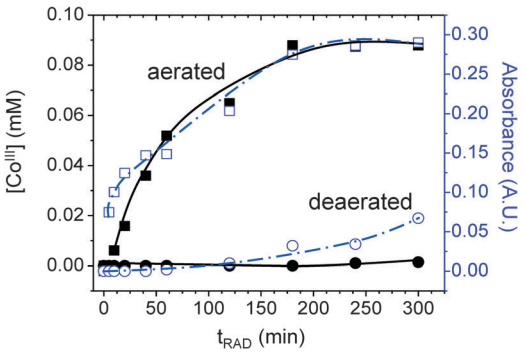

Fig. 4 Concentration of Co^{III}(sol) as a function of irradiation time for aerated (squares) and deaerated (circles) solutions initially containing 0.3 mM Co^{II}(sol) at pH 10.6. The concentrations were determined by the PAR method (solid symbols) and UV-Vis absorbance (open symbols).

increases with irradiation time and then reaches a steady-state value after the test solution has been irradiated for approximately 55 min. This discrepancy is attributed to the loss of cobalt that has settled as a solid precipitate at the bottom of the test vial (Fig. 2).

3.2 Particle analyses

The colloid particles formed by γ-irradiation of the Co^{II} solutions were collected for various particle analyses. Solid particles of $Co(OH)_2$ formed in aerated solutions at pH 10.6 without irradiation were also collected for analysis. The TEM images of the particles formed as a function of t_{RAD} are shown in Fig. 6. The TEM images show the presence of two types of particles that have very different sizes. The larger particles are ~200 nm in width and have a thin hexagonal shape. These particles are present in non-irradiated solutions and in irradiated solutions at irradiation times < ~60 min. At longer irradiation times, few of these particles are present. They are replaced by smaller particles, 8–20 nm in size and spherical in shape.

The particles were further examined by XPS and Raman spectroscopy to determine their chemical and phase composition.

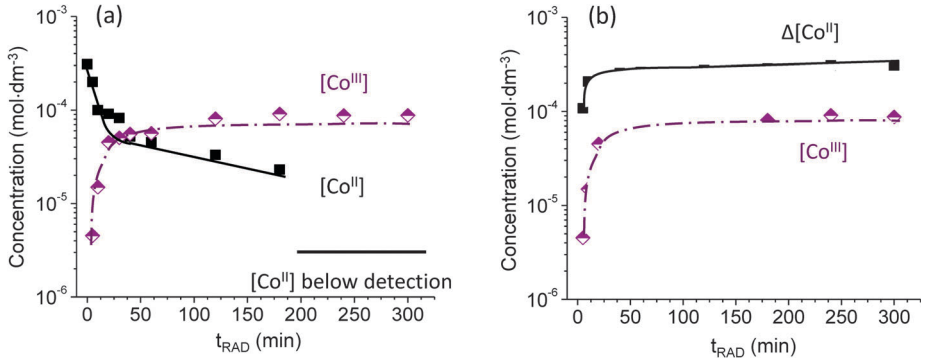

Fig. 5 (a) Concentrations of Co^{II}(sol) and Co^{III}(sol) as a function of irradiation time. (b) The $\Delta[Co^{II}(sol)]$ and $[Co^{III}(sol)]$ in the irradiated solutions initially containing 0.3 mM Co^{II}(sol) under air-saturated pH 10.6 conditions.

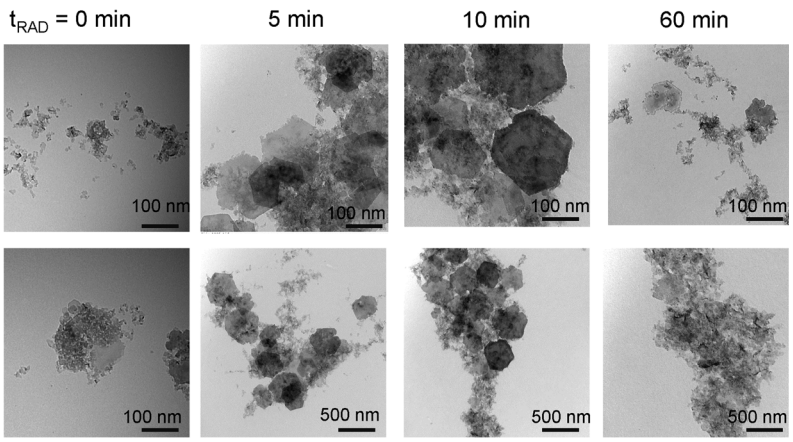

Fig. 6 TEM images of the particles collected at different irradiation times from aerated solutions initially containing 0.3 mM Co^{II}(sol) at pH 10.6.

Typical high resolution XPS spectra of the regions containing the O 1s, C 1s and Co 2p bands are shown in Fig. 7. The high resolution XPS spectra of the Co 2p band were deconvoluted using reference spectra of standard single-phase samples of Co^0, $Co(OH)_2$, CoO, Co_3O_4, CoOOH, and $CoCr_2O_4$ (which have binding energies of 778.1 eV, 780.4 eV, 780.0 eV, 779.6 eV, 780.1 eV and 778.8 eV, respectively).[31] Similarly, the O 1s and C 1s bands were deconvoluted to identify the different O components. The deconvolution of XPS bands using multiple-peak reference spectra with a Shirley-type background subtracted has been successfully applied for cobalt oxide analysis.[31] Commercial software (CASAXPS®) was used for the deconvolution fitting analysis. The weighting factors yield the relative concentrations of individual species in the Co oxide particles and the results are summarized in Fig. 8. It should be noted that the analysis depth of the XPS instrument is 6–7 nm so that the derived compositions strictly apply only to the outer layer of the particles. The XPS results show that the fraction of $Co(OH)_2$ in the particle decreases with irradiation time while the fraction of Co_3O_4 increases. The fraction of the particle that is CoOOH initially increases, reaching a maximum at ~50 min, and then decreases. The particles collected from the solutions irradiated for long times (>300 min) contain only Co_3O_4. The XPS analyses of particles collected from test solutions that were not subjected to irradiation show that they contain ~80% $Co(OH)_2$ and ~20% CoOOH. This composition did not change with time over a period of a few weeks.

The Raman spectra of particles formed as a function of irradiation time are shown in Fig. 9. We could not establish the analysis depth of Raman spectroscopy, but it is generally considered to be deeper than the XPS technique (in the order of the wavelength of the exciting line depending on the absorption properties of the material).[32] Comparison of the Raman spectra of the particles from irradiated tests with the reference spectra of different Co oxides (Fig. 9b) also shows that the particles are composed of only Co_3O_4. A broad band centered at 3000 cm^{-1} (full width of the peak not shown in Fig. 9) grows at short irradiation times and then decreases. The origin of this band is not clear but may be attributed to the fluorescence of Co_3O_4, since the broad band also appears in the reference spectrum of Co_3O_4 and the Raman excitation laser wavelength (633 nm) is on the edge of the UV-Vis absorption band. It is not clear why this band disappears at longer irradiation times, but it could be that changes in particle size may change the absorption cross section at the excitation wavelength.

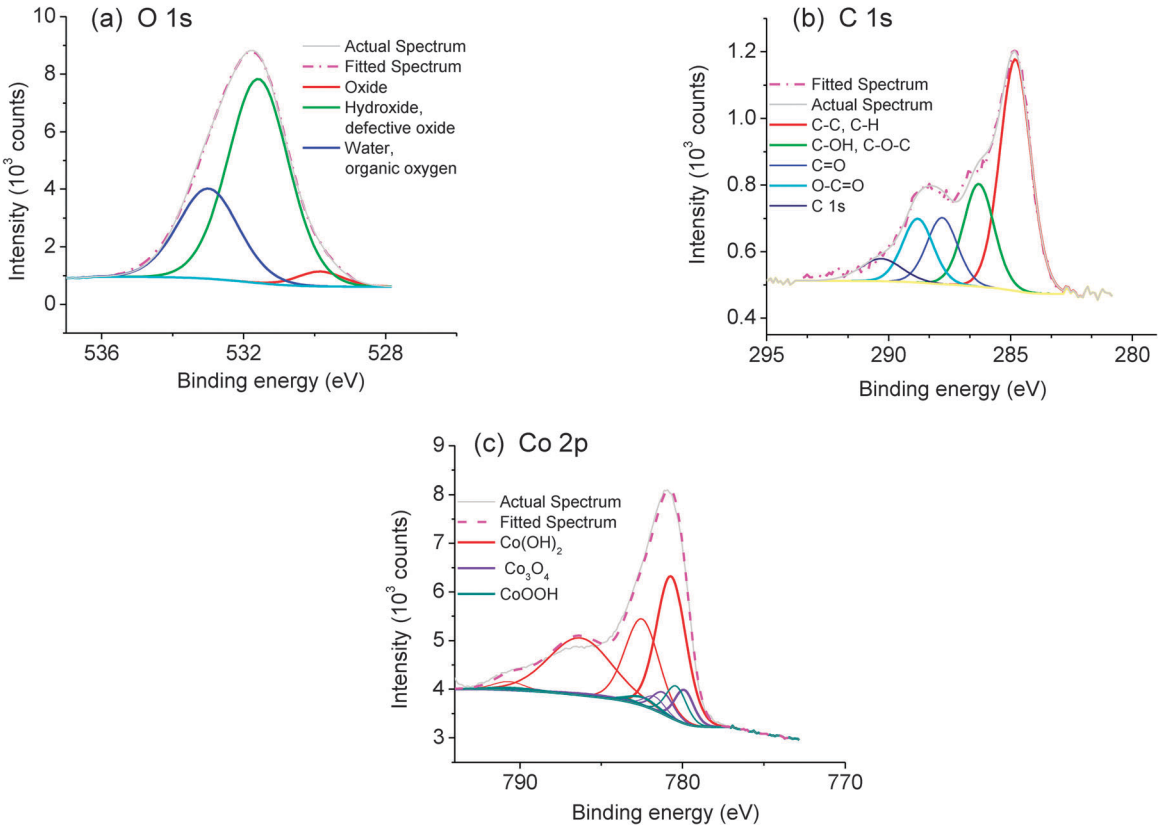

Fig. 7 High resolution XPS spectra of the (a) O 1s, (b) C 1s, and (c) Co 2p bands obtained from particles collected after 5 min of irradiation of a deaerated solution initially containing 0.3 mM Co^{II}(sol) at pH 10.6. Deconvoluted reference spectra and the composite spectra are also shown.

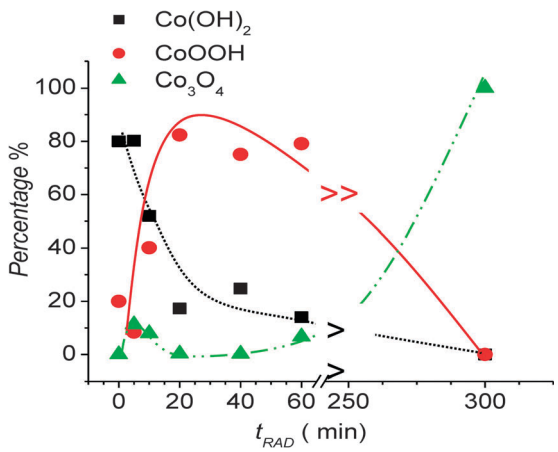

Fig. 8 Composition determined by XPS of particles collected as a function of irradiation time from aerated solutions initially containing 0.3 mM Co^{II}(sol) at pH 10.6.

3.3 Effects of pH and dissolved oxygen

The solution pH and dissolved oxygen concentration affect the net radiolytic production of H_2O_2 and H_2 under long-term steady-state irradiation even in the absence of other dissolved species.[25] In the absence of any cobalt ions, the net radiolytic production of H_2O_2 as a function of t_{RAD} in aerated solution is similar at both pHs, see Fig. 10. The presence of Co^{II}(sol) in aerated solution does not significantly affect $[H_2O_2]$ at pH 6.0, but significantly reduces $[H_2O_2]$ below 3 μM (our detection limit) at pH 10.6 at all times (>5 min, our first measurement time). The presence of Co^{II}(sol) in solution also lowers $[H_2]$ in an aerated solution but not as dramatically. In deaerated solutions (results not shown), $[H_2O_2]$ is still below the detection limit at all irradiation times while $[H_2]$ is the same as that observed for pure water.

The large change in $[H_2O_2]$ with Co^{II} present indicates that H_2O_2 (and its oxidizing radiolysis product precursors) is involved in a reaction with Co^{II}(sol). However, since conversion of Co^{II}(sol) to Co^{III}(sol) was not observed at pH 6.0 (where equal concentrations of radiolytic H_2O_2 are normally present), the oxidation of Co^{II} to Co^{III} observed at pH 10.6 must have an additional requirement. We believe that this requirement is the existence of a solid surface on which a heterogeneous oxidation process can occur. The solid surface is initially created by the nucleation and condensation of $Co(OH)_2$ from the solution. The $Co(OH)_2$ is formed by hydrolysis of the Co^{II} initially introduced into the solution as dissolved $CoSO_4$:

$$Co^{2+} + OH^- \leftrightarrows Co(OH)^+ \quad (2a)$$

$$Co(OH)^+ + OH^- \leftrightarrows Co(OH)_2 \quad (2b)$$

$$Co(OH)_2 + OH^- \leftrightarrows Co(OH)_3^- \quad (2c)$$

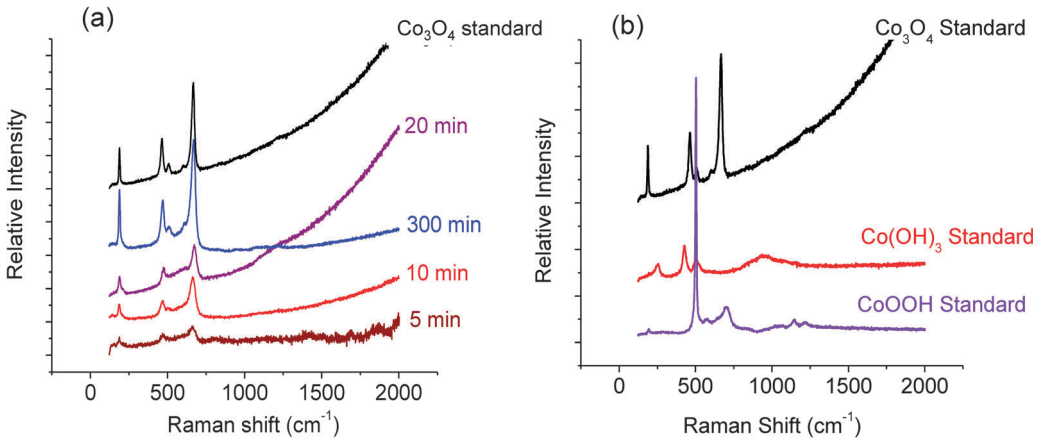

Fig. 9 (a) Raman spectra of particles collected as a function of irradiation time from aerated solutions initially containing 0.3 mM Co^{II}(sol) at pH 10.6. (b) Raman spectra of particles prepared from several pure cobalt oxides.

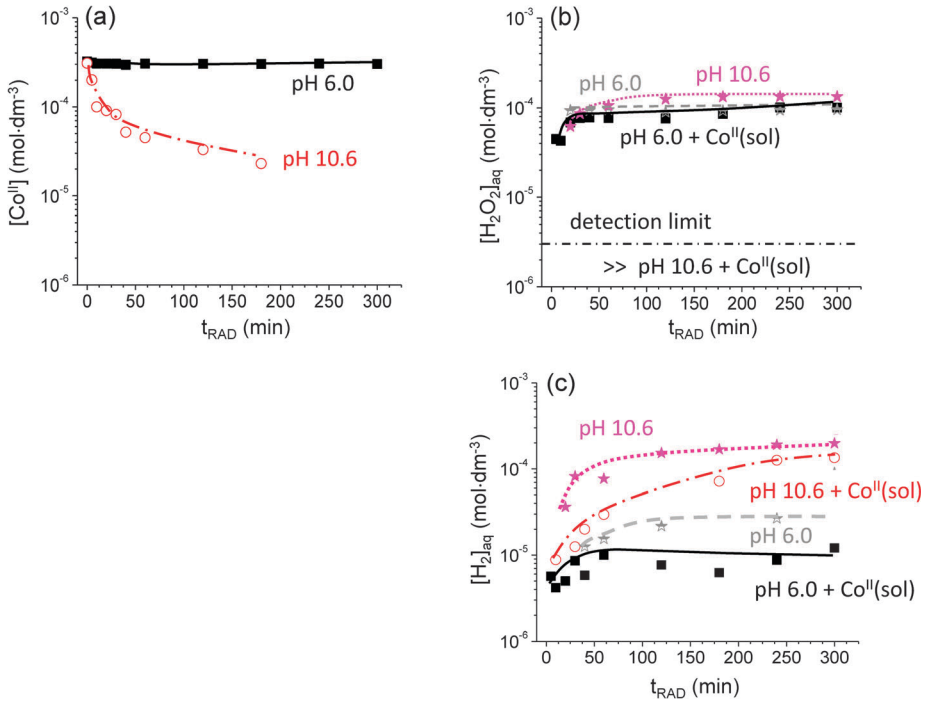

Fig. 10 Concentrations of (a) [Co^{II}(sol)], (b) [H_2O_2] and (c) [H_2] as a function of irradiation time at pHs 6.0 and 10.6 aerated solutions initially containing 0.3 mM Co^{II}(sol). The [H_2O_2] and [H_2] as a function of irradiation time in pure water are also shown for comparison.

The overall solubility and the contributions of the various Co^{II} hydrolysis species to the solubility were calculated as a function of pH based on Baes and Mesmer[27] and are shown in Fig. 11. The overall solubility of these hydrolyzed Co^{II} species is low at pH 10.6 ($\sim 10^{-6}$ M). The solution will be quickly supersaturated with hydrolyzed Co^{II} species and excess Co^{II} species will condense as solid $Co(OH)_2$ when starting with $\sim$0.3 mM $CoSO_4$ solution. Ionic Co^{II} species are easily adsorbed on the surface of the condensation nucleus and condensed $Co(OH)_2$ is more likely to form stable nucleates or clusters of Co^{II} species ($Co_x(OH)_{2y}^{(x-y)+}$) dispersed in solution. Because particles do not grow, we could not collect any particles when the test solutions were initially deaerated.

The presence of an oxidizing agent (O_2) in aerated solutions allows a small fraction of the initial clusters of $Co_x(OH)_{2y}^{(x-y)+}$ to oxidize to Co^{III} and form nearly insoluble CoOOH:

$$4Co(OH)_2 + O_2 \leftrightarrows 4CoOOH + 2H_2O \qquad (3)$$

The solubility of CoOOH is negligible at all pHs.[27] The formation and precipitation of CoOOH accelerates agglomeration of the $Co_x(OH)_{2y}^{(x-y)+}$ clusters in solution. The result can be

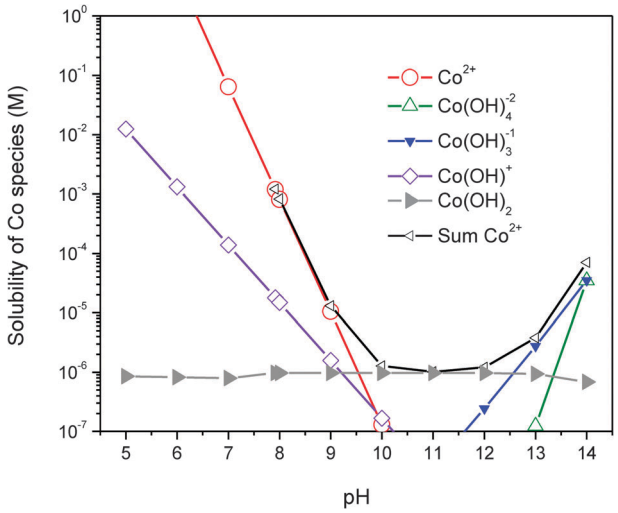

Fig. 11 Overall solubility of Co^{II} hydroxide as a function of pH and the concentrations of the contributing hydroxide species.

seen in the TEM image (Fig. 6) and XPS analysis (Fig. 7) of the particles collected from aerated test solutions without irradiation. The TEM image of the particles collected at t_{RAD} = 0 min shows small particulates congregated in a hexagonal shape and XPS analysis identifies them mostly as $Co(OH)_2$ with a small fraction as CoOOH. At pH 6.0 the solubility of Co^{II} is sufficiently high (Fig. 11) that no condensation (or precipitation) was observed.

At pH 10.6 we see a significant reduction in $[H_2O_2]$ in both aerated and deaerated irradiated solutions (Fig. 10b) although the conversion of Co^{II}(sol) to Co^{III}(sol) is much slower in deaerated solutions (Fig. 4). These observations can be explained by the difference in the rate of reduction of CoOOH to $Co(OH)_2$ in aerated *versus* deaerated solutions. Upon exposure to γ-irradiation, the Co^{II}(sol) or Co^{II} adsorbed on the particles will be quickly oxidized to CoOOH by $^{\bullet}OH$ and H_2O_2:

$$Co^{II}(sol) + {}^{\bullet}OH \rightarrow [Co(OH)_3] \rightarrow CoOOH + H_2O \quad (4)$$

$$2Co(OH)_2 + H_2O_2 \rightarrow [2Co(OH)_3] \rightarrow 2CoOOH + 2H_2O \quad (5)$$

The electrochemical equilibrium potential for the $Co(OH)_2$ and CoOOH redox reaction (reaction (6c)) is relatively high, 0.36 V_{SHE} at pH 10.6, where V_{SHE} is the potential with respect to standard hydrogen electrode potential.[22] The Co^{II}/Co^{III} equilibrium potential is still lower than the equilibrium potentials for the redox reactions of $OH^-/{}^{\bullet}OH$ and OH^-/H_2O_2, and hence Co^{II} can be oxidized by $^{\bullet}OH$ and H_2O_2. However, H_2O_2 can also oxidize to O_2, reaction (6b). This reaction can thus couple with the reduction of CoOOH (6a):

$$2CoOOH + 2H^+ + 2e^- \leftrightarrows 2Co(OH)_2 \quad (6a)$$

$$H_2O_2 \leftrightarrows O_2 + 2H^+ + 2e^- \quad (6b)$$

$$\text{Net: } 2CoOOH + H_2O_2 \leftrightarrows 2Co(OH)_2 + O_2 \quad (6c)$$

The standard potential for equilibrium 6a is E^o = 0.695 V_{SHE}.[33] The equilibrium (or Nernst) potential depends on pH and the concentrations of H_2O_2 and dissolved O_2. At pH 10.6, the equilibrium potential for the H_2O_2 oxidation equilibirum is ~0.20 V_{SHE} when $[O_2]/[H_2O_2] = 10^{-3}$ and ~0.38 V_{SHE} when $[O_2]/[H_2O_2]$ = 1. Thus, at a low dissolved oxygen concentration, the equilibrium potential for (6a) lies below that of $Co(OH)_2$/CoOOH. That shifts the equilibrium (6c) to the right and the net production of CoOOH will be slow, and so will be the subsequent irreversible conversion of CoOOH to Co_3O_4. Consequently we did observe any Co_3O_4 formation in deaerated solutions. At a higher $[O_2]$ the equilibrium of reaction (6c) shifts to the left. The net production of CoOOH is increased in aerated solutions, and we in turn see production of Co_3O_4.

The mixed $Co^{II/III}$ oxide, Co_3O_4, is thermodynamically more stable than CoOOH. However, the oxidation of $Co(OH)_2$ to CoOOH is kinetically more facile than oxidation to Co_3O_4. Thus, CoOOH will be formed first. At longer times CoOOH will be converted to the thermodynamically more stable Co_3O_4 by irreversible processes such as polycondensation of CoOOH and $Co(OH)_2$:

$$2CoOOH + Co(OH)_2 \leftrightarrows Co_3O_4 + 2H_2O \quad (7)$$

The conversion of CoOOH to Co_3O_4 is also accelerated by the radiolytic reduction of CoOOH, reaction (8), coupled with reaction (6a), resulting in the net reaction (9):

$$3CoOOH + H^+ + e^- \leftrightarrows Co_3O_4 + 2H_2O. \quad (8)$$

$$6CoOOH + H_2O_2 \leftrightarrows 2Co_3O_4 + O_2 + 4H_2O. \quad (9)$$

The reactions of H_2O_2 with cobalt species (reactions (5), (6) and (8)) are similar to the Fenton reactions with iron species.[34] We think the Fenton-like reaction occurs more readily under irradiation since the semi-conducting oxide nanoparticles become conducting due to photons with a wide range of energy. The band gap of CoO/Co_3O_4 has been reported to be in a range of 1.4–2.1 eV[35] and electrocatalytic properties of cobalt oxides[36,37] have been reported in the literature.

3.4 Reaction of H_2O_2 with Co^{II} under un-irradiated conditions

To isolate the role of H_2O_2 from that of $^{\bullet}OH$ as an oxidizing agent, the reaction of Co^{II} and H_2O_2 was studied as a function of $[H_2O_2]$ in a range of 0.1 mM to 10 mM in aerated or deaerated solutions at pH 10.6 with no radiation present. For all test conditions, even after a few weeks of reaction time, we could not detect the formation of any Co_3O_4 particles by the PAR method, TEM or XPS. These results confirm that some radiolysis product, and most likely the hydroxyl radical, is necessary in the mechanism to form cobalt oxide nanoparticles. Normally radical species are not very effective in participating in reactions on particle surfaces due to their low concentrations and the distances required to diffuse to a particle surface. However, under γ-irradiation, nanometersized colloid particles will be evenly dispersed in the solution and $^{\bullet}OH$ is produced continuously and uniformly throughout the solution. Thus, $^{\bullet}OH$ does not have to diffuse far to reach the particle interface where it can react to form Co^{III} species which can then adsorb

on the particle. Hydrogen peroxide is also involved in the oxidation of hydrated Co^{II} in the aqueous phase or on the surface of the $Co_x(OH)_{2y}^{(x-y)+}$ clusters (reaction (5)). However, H_2O_2 is also equally effective in reducing Co^{III} back to hydrated Co^{II} (reaction (6)) but the net rate of reduction is greatly reduced with O_2 present. The conversion of hydrated Co^{II} and CoOOH is fast due to the reactions (4) and (5) under irradiation, and their concentrations reach pseudo equilibrium. Once formed CoOOH is irreversibly converted to Co_3O_4 *via* reactions (7) and (9). Reaction (7) is, however, slow, whereas surface reduction of CoOOH to Co_3O_4 by H_2O_2 (reaction (9)) is fast. Hydrogen peroxide alone cannot produce enough CoOOH to form Co_3O_4, and consequently no particle formation is observed in the absence of radiation.

3.5 Kinetic behaviour of radiolysis products, H_2O_2 and H_2

Previous radiolysis kinetic studies[25,38,39] have shown that the concentration of H_2 produced by continuous γ-radiolysis is determined mainly by the primary radiolysis production rate of H_2 (the primary yield for H_2 given in reaction (1) multiplied by the dose rate) and the rate of its reaction with $^{\bullet}OH$:

$$H_2 + {}^{\bullet}OH \rightarrow H_2O + H^{\bullet} \quad k_{10} = 2.3 \times 10^8\ M^{-1}\ s^{-1} \tag{10}$$

The decrease in $[H_2]$ in irradiated solutions of Co^{II}(sol) (Fig. 10) thus indicates that there is an increase in $[^{\bullet}OH]$ in the solutions. This increase in $[^{\bullet}OH]$ is attributed to a decrease in $[H_2O_2]$. In addition to reaction with H_2 (reaction (10)), $^{\bullet}OH$ reacts with Co^{II}, $^{\bullet}O_2^-$, and H_2O_2:[40]

$$Co^{2+} + {}^{\bullet}OH \rightarrow Co^{3+} + OH^- \quad k_{11} = 1.6 \times 10^6\ M^{-1}\ s^{-1} \tag{11}$$

$$^{\bullet}OH + {}^{\bullet}O_2^- \rightarrow O_2 + OH^- \quad k_{12} = 8 \times 10^9\ M^{-1}\ s^{-1} \tag{12}$$

$$^{\bullet}OH + H_2O_2 \rightarrow HO_2^{\bullet} + H_2O \quad k_{13} = 2.7 \times 10^7\ M^{-1}\ s^{-1} \tag{13}$$

The presence of Co^{II} in solution will decrease the $[H_2O_2]$ due to reactions (5), (6) and (9). A decrease in $[H_2O_2]$ leads to a reduction in the rate of reaction (13). This compensates for the rate of loss of $^{\bullet}OH$ due to reaction (4) (or 11) and causes an increase in $[^{\bullet}OH]$ which then causes a decrease in $[H_2]$.

4. Mechanism of radiolytic production of Co_3O_4 nanoparticles

4.1 Mechanism for Co_3O_4 nanoparticle formation

A mechanism for Co_3O_4 particle formation that is consistent with all of the observations is summarized schematically in Fig. 12. Radiation-induced formation of Co_3O_4 nanoparticles requires the presence of stable nucleates of Co^{II} species ($Co_x(OH)_{2y}^{(x-y)+}$). Upon exposure to γ-irradiation, the Co^{II} adsorbed on the nucleates will be quickly oxidized to CoOOH by the oxidizing radiolysis products $^{\bullet}OH$ and H_2O_2, *via* reactions (4) and (5). The CoOOH then undergoes polycondensation with $Co(OH)_2$ to form Co_3O_4. The conversion of CoOOH to Co_3O_4 is accelerated in the presence of H_2O_2 *via* reaction (9). The proposed mechanism can explain the pH dependence (*via* its influence on the formation of Co^{II} nucleates), and the dissolved oxygen dependence of the process (*via* its influence on the stability of H_2O_2 (reaction (6b))) and the observed behaviour of water radiolysis products of H_2 and H_2O_2.

4.2 Comparison of the mechanisms for cobalt and iron systems

Our previous studies on the radiolytic formation of iron oxide colloids from dissolved ferrous ions have shown that oxidation of Fe^{II}(aq) to less soluble $Fe(OH)_3$ provides nucleation sites for particle growth and that this oxidation is very fast.[26] Compared to the analogous cobalt reaction (11), the rate of Fe^{II}(aq) reaction with $^{\bullet}OH$ is two order of magnitude higher with a rate constant of $2.3 \times 10^8\ M^{-1}\ s^{-1}$.[40] Likewise, the net oxidation of Fe^{II} by H_2O_2 is faster than the similar oxidation of Co^{II} as discussed earlier. Subsequently ferrous ions are continuously adsorbed and oxidized on the nucleates, growing them into nano-scale γ-FeOOH particles. The final size and morphology of the particles is regulated by the radiolytically induced steady-state redox conditions at the water–solid particle interface and the phase of the oxide.

The cobalt system behaves similarly to the iron system in the sense that the formation of the final nanoparticles occurs *via* an

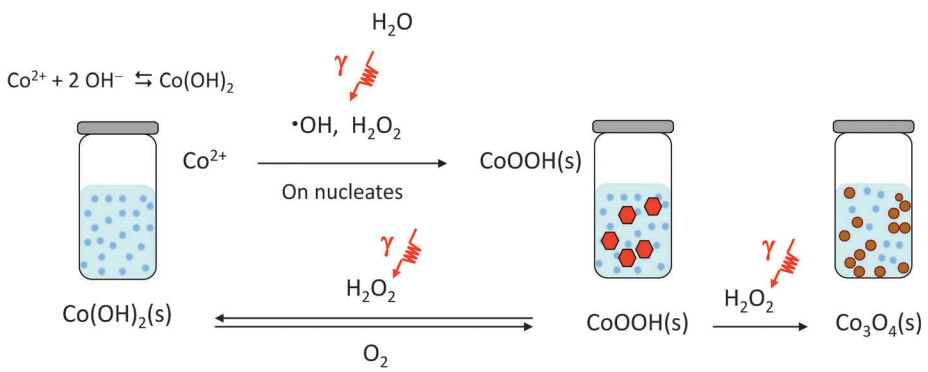

Fig. 12 Schematic of the mechanism proposed for radiation-induced cobalt oxide colloid formation.

oxidation process, oxidation of the Co^{II}(sol) to CoOOH in the case of cobalt. The differences between particle formation process for the two transition metals lie with the particle nucleation stage. In the case of cobalt, the presence of O_2 in solution is required to drive the formation of insoluble CoOOH. For iron this oxidation step is not required and radiolytic oxidation of Fe^{II} to less soluble $Fe(OH)_3$ provides nucleation sites. The radiolytic conversion of Co^{II}(sol) to insoluble Co^{III}oxides/hydroxides is also slower than the production of insolution iron species due to the high redox potential of this process for Co. Direct oxidation of Co^{II} by O_2 is therefore required to supplement slow radiolytic oxidative production of nucleates in the cobalt system. Thus, for the cobalt system, the Co^{II} clusters formed at high pH act as the nucleation sites on which further oxidation of Co^{II}(sol) to CoOOH occurs.

For the iron system, even though the initial nucleation step is fast and the growth of dendritic γ-FeOOH particles is also fast ($\leq$60 min), the conversion of γ-FeOOH to the thermodynamically more stable Fe_3O_4 is slow due to the stability of γ-FeOOH. Hence we did not observe Fe_3O_4 formation in irradiation tests lasting 300 min. In contrast, for cobalt the reduction of CoOOH to Co_3O_4 (reaction (8)) can be effectively coupled with the oxidation of H_2O_2 to O_2 (reaction (6b)) and we see the conversion of CoOOH to Co_3O_4 within 300 min of irradiation time.

5. Conclusion

Our study demonstrates that radiolysis of dilute cobalt solutions can produce highly uniform, nanometer-sized cobalt oxide particles. The particle formation process has implications for those interested in controlling or removing dissolved cobalt from water systems. The particle formation process has the potential to be used as a practical method of production of cobalt nanoparticles for many applications.

At high pHs, the presence of insoluble $Co(OH)_2$ in an aerated solution subjected to gamma irradiation creates nucleation sites on which further oxidation of Co^{II} by the water radiolysis products ($^{\bullet}OH$, H_2O_2) can occur. The resulting CoOOH then rapidly converts to more stable Co_3O_4 nanoparticles. The formation of the nanoparticles is accelerated by the presence of O_2 in solution as this drives an equilibrium that favours the formation of CoOOH.

A key difference controlling the particle formation process in the iron and cobalt systems is the electrochemical potential of the oxidation of M^{2+} to M^{3+}. This influences the rate of formation of insoluble M^{3+} nucleation sites on which further oxidation can occur leading to the formation of metal oxide nanoparticles.

Acknowledgements

This work was funded under the NSERC (Natural Science and Engineering Research Council of Canada) Discovery grant. Support from the Canada Foundation for Innovation New Opportunity grant and the Ontario Research Fund Excellence in Research: Nuclear Ontario grant is greatly acknowledged for the purchase of the UV-Vis absorption and FTIR spectrometers, respectively. L. M. Alrehaily would like to thank the Ministry of Higher Education in Saudi Arabia for the funding of her graduate study. The authors would also like to acknowledge Dr Richard Gardiner at the Western University Biotron Facility Electron Microscopy for his assistance with TEM imaging.

References

1 M. M. Rahman, J. Z. Wang, X.-L. Deng, Y. Li and H.-K. Liu, *Electrochim. Acta*, 2009, **55**, 504.
2 Y. Zhang, Y. Chen, T. Wang, J. Zhou and Y. Zhao, *Microporous Mesoporous Mater.*, 2008, **114**, 257.
3 E. Papis, F. Rossi, M. Raspanti, I. Dalle-Donne, G. Colombo, A. Milzani, G. Bernardini and R. Gornati, *Toxicol. Lett.*, 2009, **189**, 253.
4 S. Mandal, S. Phadtare and M. Sastry, *Curr. Appl. Phys.*, 2005, **5**, 118.
5 Q. A. Pankhurst, J. Cononolly, S. K. Jones and J. Dobson, *J. Phys. D: Appl. Phys.*, 2003, **36**, R167.
6 L. LaConte, N. Nitin and G. Bao, *Nano Today*, 2005, **19**, 32.
7 A. Ito, M. Shinkai, H. Honda and T. Kobayashi, *J. Biosci. Bioeng.*, 2005, **100**, 1.
8 Y. Ikedo, J. Sugiyama, H. Nozaki, H. Itahara, J. H. Brewer, E. J. Ansaldo, G. D. Morris, D. Andreica and A. Amato, *Phys. Rev. B: Condens. Matter*, 2007, **75**, 054424.
9 C. S. Cheng, M. Serizawa, H. Sakata and T. Hirayama, *Mater. Chem. Phys.*, 1998, **53**, 225.
10 M. Ando, T. Kobayashi, S. Iijima and M. Haruta, *J. Mater. Chem.*, 1997, **7**, 1779.
11 C. Pirovano and S. Trasatti, *J. Electroanal. Chem.*, 1984, **180**, 171.
12 S. Sakamoto, M. Yoshinaka, K. Hirota and O. Yamaguchi, *J. Am. Ceram. Soc.*, 1997, **80**, 267.
13 V. R. Shinde, S. B. Mahadik, T. P. Gujar and C. D. Lokhande, *Appl. Surf. Sci.*, 2006, **252**, 7487.
14 K. Shalini, A. U. Mane, S. A. Shivashankar, M. Rajeswari and S. Choopun, *J. Cryst. Growth*, 2001, **231**, 242.
15 L. M. Parkes, R. Hodgson, L. T. Lu, L. D. Tung, I. Robinson, D. G. Fernig and N. T. Thanh, *Contrast Media Mol. Imaging*, 2008, **3**, 150.
16 Z. W. Zhao, K. Konstantinov, L. Yuan, H. K. Liu and S. X. Dou, *J. Nanosci. Nanotechnol.*, 2004, **4**, 861.
17 C. S. Cheng, M. Serizawa, H. Sakata and T. Hirayama, *Mater. Chem. Phys.*, 1998, **53**, 255.
18 A. U. Mane, K. Shalini, A. Wohlfart, A. Devi and S. A. Shivashankar, *J. Cryst. Growth*, 2002, **240**, 157.
19 S. R. Ahmed, S. B. Ogale, R. Ramesh, G. C. Papaefthymiou and P. Kofinas, *Appl. Phys. Lett.*, 2002, **80**, 1616.
20 F. Švegl, B. Orel, I. Grabec-Švegl and V. Kaučič, *Electrochim. Acta*, 2000, **45**, 4359.
21 R. J. Woods and A. K. Pikaev, *Applied Radiation Chemistry: Radiation Processing*, John Wiley & Sons, Inc., New York, 1994.
22 M. Behazin, M. C. Biesinger, J. J. Noël and J. C. Wren, *Corros. Sci.*, 2012, **63**, 40.
23 J. W. T. Spinks and R. J. Woods, *An Introduction to Radiation Chemistry*, Wiley, New York, 1990.
24 J. C. Wren, *ACS Symposium Series*, American Chemical Society, Washington, DC, 2010, p. 271.
25 J. M. Joseph, B.-S. Choi, P. A. Yakabusie and J. C. Wren, *Radiat. Phys. Chem.*, 2008, **77**, 1009.
26 P. A. Yakabuskie, J. M. Joseph, P. Keech, G. A. Botton, D. Guzonas and J. C. Wren, *Phys. Chem. Chem. Phys.*, 2011, **13**, 7198.
27 *Hydrolysis of Cations*, ed. C. F. Baes and R. E. Mesmer, Krieger Pub. Co., 1986.
28 T. Yotsuyanagi, R. Yamashita and K. Aomura, *Anal. Chem.*, 1972, **44**, 1091.
29 C. J. Hochanadel, *J. Phys. Chem.*, 1952, **56**, 587.
30 I. Stefanic and J. A. LaVerne, *J. Phys. Chem. A*, 2002, **106**, 447.
31 M. C. Biesinger, B. P. Payne, A. P. Grosvenor, L. W. M. Lau and A. R. Gerson, *Appl. Surf. Sci.*, 2011, **257**, 2717.
32 E. C. Le Ru and P. G. Etchegoin, *Principles of Surface-Enhanced Raman Spectroscopy*, Elsevier, 2008.

33 A. Bard and L. R. Faulkner, *Electrochemical Methods: Fundamental and Applications*, John Wiley & Sons, Inc., 2nd edn, 2001.
34 A. P. Murphy, W. J. Boegll, M. K. Price and C. D. Moody, *Environ. Sci. Technol.*, 1989, **23**, 166.
35 A. U. Mane and S. A. Shivashankar, *J. Cryst. Growth*, 2003, **254**, 368.
36 L. C. Schumacher, I. B. Holzhueter, I. R. Hill and M. J. Dignam, *Electrochim. Acta*, 1990, **35**, 975.
37 A. N. Kamkin, G. D. Zhou and A. D. Davydov, *Prot. Met.*, 2001, **37**, 64.
38 P. A. Yakabuskie, J. M. Joseph, C. Stuart and J. C. Wren, *J. Phys. Chem. A*, 2011, **115**, 4270.
39 P. A. Yakabuskie, J. M. Joseph and J. C. Wren, *Radiat. Phys. Chem.*, 2010, **79**, 777.
40 G. V. Buxton, R. M. Sellers and D. R. McCracken, *J. Chem. Soc., Faraday Trans.*, 1976, **72**, 1464.

